Advection Augmented Convolutional Neural Networks

Niloufar Zakariaei
University of British Columbia
Vancouver, Canada
`nilouzk@student.ubc.ca`

Siddharth Rout
University of British Columbia
Vancouver, Canada
`siddharth.rout@ubc.ca`

Eldad Haber
University of British Columbia
Vancouver, Canada
`ehaber@eoas.ubc.ca`

Moshe Eliasof
University of Cambridge
Cambridge, United Kingdom
`me532@cam.ac.uk`

Abstract

Many problems in physical sciences are characterized by the prediction of space-time sequences. Such problems range from weather prediction to the analysis of disease propagation and video prediction. Modern techniques for the solution of these problems typically combine Convolution Neural Networks (CNN) architecture with a time prediction mechanism. However, oftentimes, such approaches underperform in the long-range propagation of information and lack explainability. In this work, we introduce a physically inspired architecture for the solution of such problems. Namely, we propose to augment CNNs with advection by designing a novel semi-Lagrangian push operator. We show that the proposed operator allows for the non-local transformation of information compared with standard convolutional kernels. We then complement it with Reaction and Diffusion neural components to form a network that mimics the Reaction-Advection-Diffusion equation, in high dimensions. We demonstrate the effectiveness of our network on a number of spatio-temporal datasets that show their merit.

1   Introduction and Motivation

Convolution Neural Networks (CNNs) have long been established as one of the most fundamental and powerful family of algorithms for image and video processing tasks, in applications that range from image classification [25, 19], denoising [5] and reconstruction [24], to generative models [15]. More examples of the impact of CNNs on various fields and applications can be found in [38, 16, 30] and references within.

At the core of CNNs, stands the convolution operation – a simple linear operation that is local and spatially rotation and translation equivariant. The locality of the convolution, coupled with nonlinear activation functions and deep architectures have been the force driving CNN architectures to the forefront of machine learning and artificial intelligence research [46, 19]. One way to understand the success of CNNs and attempt to generate an explainable framework to them is to view CNNs from a Partial Differential Equation (PDE) point of view [40, 7]. In this framework, the convolution is viewed as a mix of discretized differential operators of varying order. The layers of the network are then associated with time. Hence, the deep network can be thought of as a discretization of a nonlinear time-dependent PDE. Such observations have motivated parabolic network design that smooth and denoise images [41] as well as to networks that are based on hyperbolic equation [26] and semi-implicit architectures [18].

However, it is known from the literature [32], and is also demonstrated in our experiments, that CNN architectures tend to under-perform in tasks that require rapid transportation (also known as

.

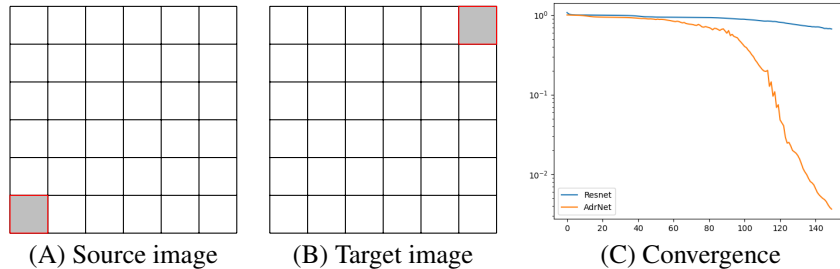| (A) Source image | (B) Target image | (C) Convergence |

Figure 1: A simple task of moving information from one side of the image to the other. The source image in A is moved to the target image in B. The convergence of a simple ResNet and an ADRnet proposed in this work is in (C).

advection) of information from one side of an image to the other. In particular, in this paper, we focus on the prediction of the spatio-temporal behavior of image features, where significant transportation is present in the data. Examples of such data include the prediction of weather, traffic flow, and crowd movement.

Related work: In recent years, significant research was devoted for addressing spatio-temporal problems. Most of the works known to us are built on a combination of CNN to capture spatial dependencies and Recurrent Neural Networks (RNN) to capture temporal dependencies. A sample of papers that address this problem and the related problem of video prediction can be found in [4, 49, 43, 29, 20, 33, 11] and reference within. See also [60] and [37] for a recent comparison between different methods. Such methods typically behave as black boxes, in the sense that while they offer strong downstream performance, they often times lack a profound understanding of the learned underlying dynamics from the data. Another type of work that is designed for the scientific datasets is [47], which uses Fourier-based methods to build the operators. See also [3] for a review on the topic.

Motivation: Notably, while a CNN is a versatile tool that allows to learn spatial dependencies, it can have significant challenges in learning simple operations that require transportation. As an example, let us consider the problem of predicting the motion in the simple case that the input data is an image, where all pixels take the value of 0 except for a pixel on the bottom left (marked in gray), and the output is an image where the value is transported to a pixel on the top right. This example is illustrated in Figure 1. Clearly, no local operation, for example, a convolution of say, 3×3 or even 7×7 can be used to move the information from the bottom left of the image to the top right. Therefore, the architecture to achieve this task requires either many convolutions layers, or, downsampling the image via pooling, where the operations are local, performing convolutions on the downsampled image, and then upsampling the image via unpooling, followed by additional convolutions to "clean" coarsening and interpolation artifacts, as is typical in UNets [39, 8]. To demonstrate, we attempt to fit the data with a simple convolution residual network and with a residual network that has an advection block, as discussed in this paper. The convergence history for the two methods is plotted in Figure 1. We see that while a residual network is incapable of fitting the data, adding an advection block allows it to fit the data to machine precision.

This set of problems, as well as the relatively poor performance it offers on data that contains advection as in simple task in Figure 1 sets the motivation for our work. Our aim is to extend the set of tools that is available in CNNs beyond simple and local convolutions. For time-dependent PDEs, it is well known that it is possible to model most phenomena by a set of advection-diffusion-reaction equations (see, e.g., [10, 9] and references within). Motivated by the connection between the discretization of PDEs and deep network [40, 7], and our observations on the shortcomings of existing operations in CNNs, we propose reformulating CNNs into three different components. Namely, (i) a pointwise term, also known as a *reaction* term, where channels interact locally. (ii) A *diffusion* term, where features are exchanged between neighboring pixels in a smooth manner. And, (iii) an *advection* term, where features are passed from pixels to other pixels, potentially not only among neighboring pixels, while preserving *feature mass or color loss*[1]. As we discuss in Section 3, the combination of diffusion and reaction is equivalent to a standard CNN. However, there is no CNN

---

[1]That is the sum of the features is constant.

mechanism that is equivalent to the advection term. Introducing this new term allows the network flexibility in cases where information is carried directly.

Contributions: The contributions of this paper are three-fold. First, we form the spatio-temporal dynamics in high dimensions as an advection-diffusion-reaction process, which is novel and has not been studied in CNNs prior to our work. Second, we propose the use of the semi-Lagrangian approach for its solution, introducing a new type of a learnable linear layer, that is sparse yet non-local. This is in contrast to standard convolutional layers, which act locally. In contrast to advection, other mechanisms for non-local interactions, require dense interactions, which are computationally expensive [53]. Specifically, our use of semi-Lagrangian methods offers a bridge between particle-based methods and convolutions [27]. Thus, we present a new operation in the context of CNNs, that we call the *push operator* to implement the advection term. This operator allows us to transport features anywhere on the image in a single step – an operation that cannot be modeled with small local convolution kernels. It is thus a simple yet efficient replacement to the standard techniques that are used to move information on an image. Third, we propose a methodology to learn these layers based on the splitting operator approach, and show that they can successfully model advective processes that appear in different datasets.

Limitations: The advection diffusion reaction model is optimal when applied to the prediction of images where the information for the prediction is somehow present in the given images. Such scenarios are often present in scientific applications. For example, for the prediction of the propagation of fluids or gasses, all we need to know is the state of the fluid now (and in some cases, in a few earlier time frames). A more complex scenario is the prediction of video. In this case, the next frame may have new features that were not present in previous frames. To this end, the prediction of video requires some generative power. While we show that our network can be used for video prediction and even obtain close to the state-of-the-art results, we observe that it performs best for scientific datasets.

2   Model Formulation

Notations and assumptions. We consider a spatio-temporal vector function of the form $\mathbf{q}(t, \mathbf{x}) = [\mathbf{q}_1(t, \mathbf{x}), \dots, \mathbf{q}_m(t, \mathbf{x})] \in \mathcal{Q}$, where $\mathcal{Q}$ is the space vector function with m channels. The function $\mathbf{q}$ is defined over the domain $\mathbf{x} \in \Omega \subseteq \mathcal{R}^d$, and time interval $[0, t_j]$. Our goal is to predict the function at time t_k for some $t_k > t_j$, given the inputs up to time j. For the problem we consider here, the time is sampled on a uniform grid with equal spacing. Below, we define the advection-diffusion-reaction system that renders the blueprint of the method proposed in this paper to achieve our goal.

Reaction-Advection-Diffusion System. Given the input function $\mathbf{q}$, we first embed it in a higher dimensional space. We denote the embedding function by $\mathbf{I} :\in \mathcal{I}$, defined as

$$\mathbf{I}(t, \mathbf{x}) = M_{\text{In}}(\mathbf{q}(t, \mathbf{x}), \boldsymbol{\theta}_{\text{In}}) \tag{1}$$

where $M_{\text{In}} : \mathbb{R}^m \to \mathbb{R}^c$ is a multi-layer preceptron (MLP) that embeds the function $\mathbf{q}$ from m to $c > m$ channels with trainable parameters $\boldsymbol{\theta}_{\text{In}}$.

To represent the evolution of $\mathbf{q}$ we evolve $\mathbf{I}$ in the hidden dimension, c, and then project it back into the space $\mathcal{Q}$. One useful way to represent the evolution of a spatio-temporal process is by combining three different processes, as follows:

- *Reaction:* A pointwise process where channels interact pointwise (sometimes referred to as 1×1 convolutions)

- *Diffusion:* A process where features are being communicated and diffused locally.

- *Advection:* A process where information transports along mediums.

These three processes are also illustrated in Figure 2 and their composition defines the advection-diffusion-reaction differential equation on the embedded vector $\mathbf{I}$.

Advection: $t_k \rightarrow t_{k+1/3}$ Diffusion: $t_{k+1/3} \rightarrow t_{k+2/3}$ Reaction: $t_{k+2/3} \rightarrow t_{k+1}$
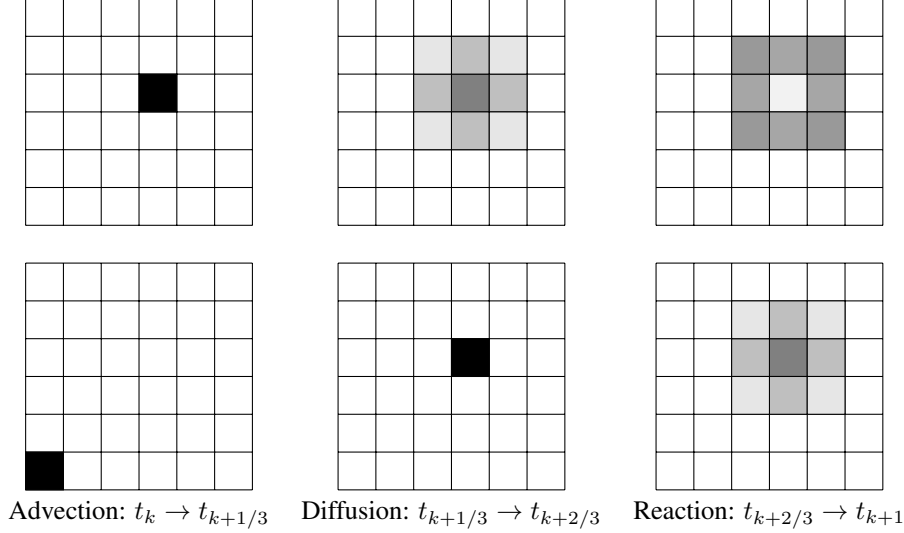
Figure 2: An illustration of the advection-diffusion reaction process. In the first step (advection), a pixel on the lower left of the image is transported into the middle of the mesh. In the second step (diffusion), the information is diffused to its neighbours and finally, in the last step (reaction) each pixel interact locally to change its value.

The equation can be written as

$$\frac{\partial \mathbf{I}(t, \mathbf{x})}{\partial t} = \kappa \Delta \mathbf{I}(t, \mathbf{x}) + \nabla \cdot (\mathbf{U} \mathbf{I}(t, \mathbf{x})) + R(\mathbf{I}(t, \mathbf{x}), \boldsymbol{\theta}), \tag{2}$$

$$\mathbf{I}(t = 0, \mathbf{x}) = M(\mathbf{q}(t = 0, \mathbf{x})). \tag{3}$$

Here Δ is the Laplacian and ∇ is the divergence operator, as classically defined in PDEs [10]. The equation is equipped with an initial condition and some boundary conditions. Here, for simplicity of implementation, we choose the Neumann boundary conditions, but other boundary conditions can also be chosen. The diffusivity coefficient κ, velocity field $\mathbf{U}$, and the parameters that control the reaction term R are trainable, and are discussed in Section 3.

The equation is integrated on some interval $[0, T]$ and finally one obtains $\mathbf{q}(T, \mathbf{x})$ by applying a second MLP, that projects the hidden features in $\mathbf{I}(t = T, \mathbf{x})$ to the desired output dimension, which in our case is the same as the input dimension, i.e., m:

$$\mathbf{q}(T, \mathbf{x}) = M_{\text{Out}}(\mathbf{I}(T, \mathbf{x}), \boldsymbol{\theta}_{\text{Out}}), \tag{4}$$

where $\boldsymbol{\theta}_{\text{out}}$ are trainable parameters for the projection MLP.

Remark (Equation 2 Reformulation). The discretization of Equation 2 can be challenging due to conservation properties of the term $\nabla \cdot (\mathbf{U} \mathbf{I}(t, \mathbf{x}))$. An alternative equation, which may be easier to discretize in our context, can be obtained by noting that

$$\frac{\partial \mathbf{I}(t, \mathbf{x})}{\partial t} + \nabla \cdot (\mathbf{U} \mathbf{I}) = \frac{\partial \mathbf{I}(t, \mathbf{x})}{\partial t} + \mathbf{U} \cdot \nabla \mathbf{I} + \mathbf{I} \nabla \cdot \mathbf{U}. \tag{5}$$

The operator on the left-hand side in Equation 5 is the continuity equation [10], where the *mass* of $\mathbf{I}$ is conserved. The first two terms on the right hand side, namely, $\mathbf{I}_t + \mathbf{U} \cdot \nabla \mathbf{I}$ are sometimes refer to as the color equation [10] as they conserve the *intensity* of $\mathbf{I}$. For divergent free velocity fields, that is, when $\nabla \cdot \mathbf{U} = 0$, these are equivalent, however, for non-divergent fields, the term $\mathbf{I} \nabla \cdot \mathbf{U}$ is a pointwise operator on $\mathbf{I}$, that is, it is a reaction term. When training a model, one can use either Equation 2 in its continuity form or replace the term with Equation 5 and learn the term $\mathbf{I} \nabla \cdot \mathbf{U}$ as a part of the reaction term, R. We discuss this in discretization of our model in Section 3.3.

3 From a Partial Differential Equation to a Neural Network

To formulate a neural network from the differential equation in Equation 2 needs to be discretized in time and space. In this work, we assume data that resides on a regular, structured mesh grid, such

as 2D images, and the spatial operators to discretize Equation 2 are described below. To discretize Equation 2 in *time*, we turn to Operator Splitting methods [1] that are common for the discretization of equations with similar structures, and were shown to be effective in deep learning frameworks [9]. As we see next, such discretization leads to a neural a network that has three types of layers that are composed of each other, resulting in an effectively deeper neural network.

3.1 Operator Splitting

The idea behind operator splitting is to split the integration of the ODE into parts [28]. Specifically, consider a linear differential equation of the form

$$\frac{\partial \mathbf{I}(t, \mathbf{x})}{\partial t} = \mathbf{A}\mathbf{I}(t, \mathbf{x}) + \mathbf{D}\mathbf{I}(t, \mathbf{x}) + \mathbf{R}\mathbf{I}(t, \mathbf{x}), \tag{6}$$

where $\mathbf{A}, \mathbf{D}$ and $\mathbf{R}$ are matrices. The solution to this system at time t is well known [10] and reads

$$\mathbf{I}(t, \mathbf{x}) = \exp\left(t\mathbf{A} + t\mathbf{D} + t\mathbf{R}\right)\mathbf{I}(0, \mathbf{x}), \tag{7}$$

where $\exp$ denotes the matrix exponentiation operation. It is also possible to approximate the exact solution presented in Equation 7 as follows

$$\exp\left(t\mathbf{A} + t\mathbf{D} + t\mathbf{R}\right)\mathbf{I}(0, \mathbf{x}) \approx \exp(t\mathbf{A})\left((\exp(t\mathbf{D})(\exp(t\mathbf{R})\mathbf{I}(0, \mathbf{x}))\right) \tag{8}$$

The approximation is of order t, and it stems from the fact that the eigenvalues of the matrices $\mathbf{A}, \mathbf{D}$ and $\mathbf{R}$ do not commute (see [1] for a thorough discussion). Equation 8 can also be interpreted in the following way. The solution, for a short time integration time t, can be approximated by first solving the system $\frac{\partial \mathbf{I}(t, \mathbf{x})}{\partial t} = \mathbf{R}\mathbf{I}(t, \mathbf{x}), \mathbf{I}_0 = \mathbf{I}(0, \mathbf{x})$ obtaining a solution $\mathbf{I}_R(t, \mathbf{x})$, followed by the solution of the system $\frac{\partial \mathbf{I}(t, \mathbf{x})}{\partial t} = \mathbf{D}\mathbf{I}_R(t, \mathbf{x}), \mathbf{I}_0 = \mathbf{I}_R$ obtaining the solution $\mathbf{I}_{RD}(t, \mathbf{x})$ and finally solving the system $\frac{\partial \mathbf{I}(t, \mathbf{x})}{\partial t} = \mathbf{A}\mathbf{I}_{RD}(t, \mathbf{x}), \mathbf{I}_0 = \mathbf{I}_{RD}$. The advantage of this approach is that it allows the use of different techniques for the solution of different problems.

Let $\mathcal{R}$ be the solution operator that advances $\mathbf{I}(t_j, \mathbf{x})$ to $\mathbf{I}_R(t_{j+1}, \mathbf{x})$. Similarly, let $\mathcal{D}$ be the solution operator that advances $\mathbf{I}_R(t_{j+1}, \mathbf{x})$ to $\mathbf{I}_{RD}(t_{j+1}, \mathbf{x})$ and lastly, let $\mathcal{A}$ be the solution of the advection problem that advances $\mathbf{I}_{RD}(t_{j+1}, \mathbf{x})$ to $\mathbf{I}(t_{j+1}, \mathbf{x})$. Then, a layer in the system can be written as the composite of three-layer

$$\mathcal{L}\,\mathbf{I}(t_j, \mathbf{x}) = \mathcal{A} \circ \mathcal{D} \circ \mathcal{R}\,\mathbf{I}(t_j, \mathbf{x}). \tag{9}$$

That is, the resulting discretization in time yields a neural network architecture of a layer that is composed of three distinct parts. We now discuss each part separately.

3.2 Advection

The innovative part of our network is advection. The advection approximately solves the equation

$$\frac{\partial \mathbf{I}}{\partial t} = \nabla \cdot (\mathbf{U}(\mathbf{I}, \mathbf{x}, t)\mathbf{I}), \tag{10}$$

for a general velocity field $\mathbf{U}$. For the solution of this equation, we now introduce a linear operation that we use to enhance the performance of our network. Our goal is to allow for information to pass over large distances. To this end, consider a displacement field $\mathbf{U} = (\mathbf{U}_1, \mathbf{U}_2)$ and consider the push operation, $\mathbf{A}(\mathbf{U})\mathbf{I}$ as the operation that takes every pixel in $\mathbf{I}$ and displaces it from point $\mathbf{x}$ to $\mathbf{x}_u = \mathbf{x} + \mathbf{U}$. Since the point $\mathbf{x}_u$ does not necessarily reside on a grid point, the information from $\mathbf{x}_u$ is spread over four grid points neighbors, in weights that are proportional to the distance from these points. A sketch of this process in plotted in Figure 3 (a). The operator discussed above conserves that *mass* of the features. A different implementation, as discussed in Remark 1, is to discretize the color equation. This is done by looking backward and using the interpolated value as shown in Figure 3(b). It is possible to show [12] that these linear operators are transposed of each other. Here, for each implementation, we chose to use the color equation. We show in ablation studies that the results when using either formulation are equivalent.

The process allows for a different displacement vector $\mathbf{u}$ for every grid point. The displacement field $\mathbf{U}$ in has $2c$ channels and can vary in space and time. To model the displacement field, we propose to use the data at times,

$$\mathbf{Q}_k = [\mathbf{q}(t_{k-j}, \mathbf{x}), \mathbf{q}(t_{k-j+1}, \mathbf{x}), \dots, \mathbf{q}(t_k, \mathbf{x})], \tag{11}$$
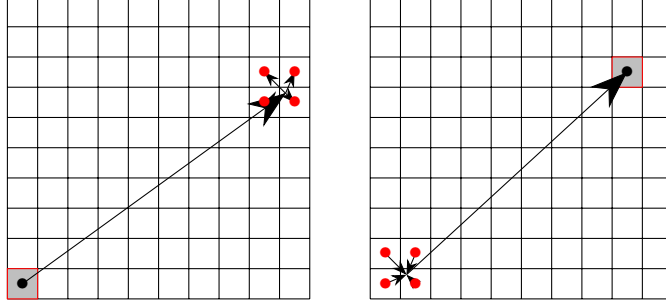
5

Figure 3: Discretization of the push operator. (a) Left: Semi-Lagrangian mass preserving transport, discretizing the continuity. (b) Right: Semi-Lagrangian color preserving transport.

where j is the length of history used to learn the displacements.

Using $\mathbf{Q}_k$, the displacement field is computed by a simple residual convolution network, which we formally write as

$$\mathbf{U}_k = RN(\mathbf{Q}_k, \boldsymbol{\eta}), \tag{12}$$

where RN is the residual network parameterized by $\boldsymbol{\eta}$.

3.3 Reaction

The reaction term is a nonlinear 1×1 convolution. This yields a residual network of the form

$$\mathbf{I}_{j+1} = \mathbf{I}_j + hM(\mathbf{I}_j, \boldsymbol{\theta}_j) = \mathcal{R}_j(\boldsymbol{\theta}_j)\,\mathbf{I}_j, \tag{13}$$

where M is a standard, double-layer MLP with parameters $\boldsymbol{\theta}_j$ and h is a step size that is a hyper-parameter. We may choose to have more than a single reaction step per iteration.

3.4 Diffusion

For the diffusion step, we need to discretize the Laplacian on the image. We use the standard 5-point Laplacian [14] that can also be expressed as 2D group convolution [35]. Let Δ_h be the discrete Laplacian. The diffusion equation reads

$$\mathbf{I}_{j+1} - \mathbf{I}_j = h\kappa\Delta_h\mathbf{I}_k.$$

If we choose $k = j$ we obtain an explicit scheme

$$\mathbf{I}_{j+1} = \mathbf{I}_j + h\kappa\Delta_h\mathbf{I}_j. \tag{14}$$

Note that the diffusion layer can be thought of as a group convolution where each channel is convolved with the same convolution and then scaled with a different κ. The forward Euler method for the diffusion requires $h\kappa$ to be small if we want to retain stability. By choosing $k = j + 1$ we obtain the backward Euler method, which is unconditionally stable

$$\mathbf{I}_{j+1} = (\mathbf{I} - h\kappa\Delta_h)^{-1}\mathbf{I}_j = \mathcal{D}(\kappa)\mathbf{I}_j. \tag{15}$$

To invert the matrix we use the cosine transform [23] which yields an $n \log n$ complexity for this step.

Combining Diffusion and Reaction to a Single Layer. In the above network the diffusion is handled by an implicit method (that is a matrix inversion) and the reaction is handled by an explicit method. For datasets where the diffusion is significant, this may be important; however, in many datasets where the diffusion is very small, it is possible to use an explicit method for the diffusion. Furthermore, since both the diffusion and reaction are computed by convolutions, it is possible to combine them into a 3×3 convolution (see [40] and [18] for a complete discussion). This yields a structure that is very similar to a classical Convolutional Residual Network that replaces the diffusion and reaction steps. For the datasets used in this paper, we noted that this modest architecture was sufficient to obtain results that were close to state-of-the-art.

3.5 Implementing the ADR Network

Implementing the diffusion and reaction terms, either jointly or combined, we use a standard Convolutional Residual Network. The advection term is implemented by using the `sampleGrid` command in pytoch, which uses an efficient library to interpolate the images.

While the network can be used as described above, we found that better results can be obtained by denoising the output of the network. To this end, we have used a standard UNet and applied it to the output. As we show in our numerical experiments, this allows us to further improve downstream performance. The complete network is summarized in Algorithm 1.

Algorithm 1 The ADR network

Set $\mathbf{I}_0 \leftarrow M(\mathbf{q}_k, \boldsymbol{\theta}_o)$, $\mathbf{Q}_k$ as in equation 11.
for $j = 0, 1, ...m - 1$ **do**
    Diffusion-Reaction $\mathbf{I}_{DR} \leftarrow \mathcal{D}_{\boldsymbol{\kappa}_j} \mathcal{R}_{\boldsymbol{\theta}_j} \mathbf{I}_j$
    Compute displacement $\mathbf{U}_j = RN(\mathbf{I}_{DR}, \boldsymbol{\eta}_j)$ as in equation 12
    Push the image $\mathbf{I}_{j+1} = \mathcal{A}(\mathbf{U}_j)\mathbf{I}_{DR}$
end for
Set $\mathbf{q}_{k+\ell} = M(\mathbf{I}_m, \boldsymbol{\theta}_T)$
(Optional) Denoise $\mathbf{q}_{k+\ell} = \text{Unet}(\mathbf{q}_{k+\ell})$

---

4 Experiments

Our goal is to develop architectures that perform well for scientific-related datasets that require advection. In our experiments, we use two such datasets, CloudCast [64], and the Shallow Water Equation in PDEbench [47]. However, our ADRNet can also be used for the solution of video prediction. While such problems behave differently than scientific datasets, we show that our ADRNet can perform reasonably well for those applications as well. Below, we elaborate on the utilized datasets. We run our codes using a single NVIDIA RTX-A6000 GPU with 48GB of memory.

4.1 Datasets

We now describe the datasets considered in our experiments, which are categorized below.

Scientific Datasets: We consider the following datasets which arise from scientific problems and communities:

- **SWE** The shallow-water equations are derived from the compressible Navier-Stokes equations. The data is comprised of 900 sets of 101 images, each of which is a time step.
- **CloudCast.** The CloudCast dataset comprises 70,080 satellite images captured every 15 minutes and has a resolution of 3712×3712 pixels, covering the entire disk of Earth.

Video Prediction Datasets: These datasets are mainly from the Computer Vision community, where the goal is to predict future frames in videos. The datasets are as follows:

- **Moving MNIST** The Moving MNIST dataset is a synthetic video dataset designed to test sequence prediction models. It features 20-frame sequences where two MNIST digits move with random trajectories.
- **KITTI** The KITTI is a widely recognized dataset extensively used in mobile robotics and autonomous driving, and it also serves as a benchmark for computer vision algorithms.

The statistics of the datasets are summarized in Table 1, and in Appendix A, we provide results on additional datasets, namely TaxiBJ [64] and KTH [42].

4.2 Evaluation

Ranking of Methods. Throughout all experiments where other methods are considered, we rank the top 3 methods using the color scheme of **First**, **Second**, and **Third**.

Table 1: Datasets statistics. Training and testing splits, image sequences, and resolutions

Dataset	N_{train}	N_{test}	(C, H, W)	$History$	$Prediction$
PDEBench-SWE	900	100	(1, 128, 128)	10	1
CloudCast	5241	1741	(1, 128, 128)	4	4, 8, 12, 16
Moving MNIST	10000	10000	(1, 64, 64)	10	10
KITTI	2042	1983	(3, 154, 512)	2	1, 3

Performance on Scientific Datasets. We start our comparisons with the SWE and CloudCast datasets. These datasets fit the description of our ADRNet as future images depend on the history alone (that is, the history should be sufficient to recover the future). Indeed, Table 2 and Table 3 show that our ADRNet performs much better than other networks for these goals.

Table 2: Results on PDEBench SWE Dataset.

Method	NRMSE ↓
UNET [48]	8.3e-2
PINN [48]	1.7e-2
MPP-AVIT-TI [34]	6.6e-3
ORCA-SWIN-B [44]	6.0e-3
FNO [48]	4.4e-3
MPP-AVIT-B [34]	**2.4e-3**
MPP-AVIT-L [34]	**2.2e-3**
ADRNet	**1.3e-4**

Table 3: Results on CloudCast dataset.

Method	SSIM (↑)	PSNR (↑)
AE-ConvLSTM [64]	**0.66**	**8.06**
MD-GAN [62]	**0.60**	**7.83**
TVL1 [52]	0.58	7.50
Persistent [64]	0.55	7.41
ADRNet	**0.83**	**38.17**

4 and Figure 5. Examples of the predictions of the SWE dataset and the CloudCast datasets are
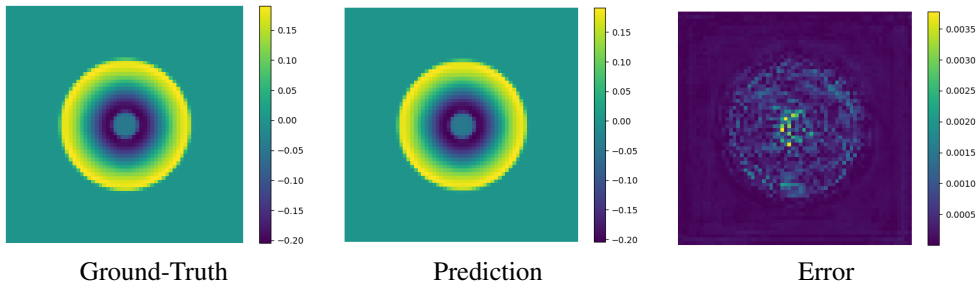

Ground-Truth   Prediction   Error

Figure 4: Prediction and error for the SWE problem using our ADRNet.

plotted in Figure For the SWE dataset, the errors are very small and close to machine precision. For CloudCast, the data is noisy, and it is not clear how well it should fit. Predicting a single-time step, while useful, has limited applicability. Our goal is to push the prediction for longer, hence providing an alternative to expensive integration. The results for SWE for long-time prediction are presented in Table 4, together with a comparison of the FNO method [31] where we see that our model performs well even for long-time prediction.

Video Prediction Performance. We have used a number of video datasets to test our ADRNet. The results of two of them (Moving MNIST and KITTI) are reported in Table 5 and Table 6. We perform additional experiments for the KTH Action and TaxiBJ datasets in the appendix A. The moving MNIST dataset adheres to the assumptions of our ADRNet. Indeed, for this dataset, we obtain results that are very close to state-of-the-art methods.

The KTH Action dataset is more complex as not all frames can be predicted from the previous frames without generation power. Nonetheless, even for this dataset our ADRNet performs close to the state of the art. This limiting aspect of video synthesis is studied through experiments in appendix A.1.

Table 4: Comparison of ADRNet and FNO across Long-Range Predictions.

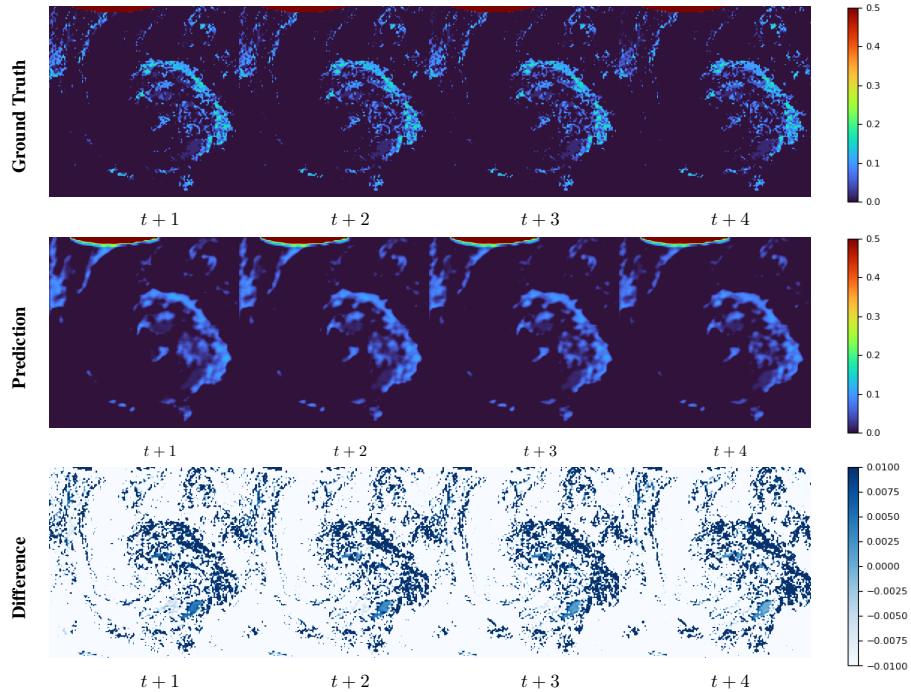| Metric	$10 \rightarrow 5$		$10 \rightarrow 10$		$10 \rightarrow 20$		$10 \rightarrow 50$	
	ADRNet	**FNO**	**ADRNet**	**FNO**	**ADRNet**	**FNO**	**ADRNet**	**FNO**
MSE $\downarrow$	9.2e-08	4.0e-07	1.5e-07	5.8e-07	2.1e-07	6.7e-07	8.5e-07	1.4e-06
nMSE $\downarrow$	8.5e-08	3.7e-07	1.4e-07	5.4e-07	1.9e-07	6.2e-07	7.8e-07	1.3e-06
RMSE $\downarrow$	3.0e-04	6.3e-04	3.9e-04	7.6e-04	4.5e-04	8.1e-04	9.2e-04	1.2e-03
nRMSE $\downarrow$	2.9e-04	6.1e-04	3.7e-04	7.3e-04	4.4e-04	7.8e-04	8.8e-04	1.1e-03
MAE $\downarrow$	2.0e-04	2.8e-04	1.7e-04	3.7e-04	1.9e-04	3.6e-04	4.1e-04	5.7e-04

Figure 5: Example of the forecast for ADRNet relative to ground truth for four time steps.

5 Conclusion

In this paper, we have presented a new network for tasks that reside on a regular mesh that can be viewed as a multi-channel image. The method combines standard convolutions with a linear operator that transports information from one part of the image to another. The transportation vector field is learned from previous images (that is, history), allowing for information to pass from different parts of the image to others without loss. We combine this information within a diffusion-reaction process that can be coded by itself or by using a standard ResNet.

Table 5: Moving MNIST.

Method	MSE ↓	MAE ↓
MSPred [54]	34.4	-
MAU [6]	27.6	-
PhyDNet [17]	24.4	70.3
SimVP [49]	23.8	68.9
CrevNet [63]	22.3	-
TAU [50]	19.8	**60.3**
SwinLSTM [51]	**17.7**	-
IAM4VP [43]	15.3	49.2
ADRNet	16.1	50.3

Table 6: Results on KITTI.

Method	MS-SSIM ($\times 10^{-2}$) ↑		LPIPS ($\times 10^{-2}$) ↓	
	$t+1$	$t+3$	$t+1$	$t+3$
SADM [2]	83.06	72.44	14.41	24.58
MCNET [55]	75.35	63.52	24.04	37.71
CorrWise [13]	82.00	N/A	17.20	N/A
OPT [61]	82.71	69.50	12.34	20.29
DMVFN [21]	88.06	76.53	10.70	19.28
DMVFN [21]	88.53	78.01	10.74	19.27
ADRNet	**85.86**	83.62	7.54	9.26

References

[1] U.M. Ascher. *Numerical methods for Evolutionary Differential Equations*. SIAM, Philadelphia, 2010.

[2] Xinzhu Bei, Yanchao Yang, and Stefano Soatto. Learning semantic-aware dynamics for video prediction. In *Proceedings of the IEEE/CVF Conference on Computer Vision and Pattern Recognition*, pages 902–912, 2021.

[3] Jan Blechschmidt and Oliver G Ernst. Three ways to solve partial differential equations with neural networks—a review. *GAMM-Mitteilungen*, 44(2):e202100006, 2021.

[4] Thomas Bohnstingl, Stanisław Woźniak, Angeliki Pantazi, and Evangelos Eleftheriou. Online spatio-temporal learning in deep neural networks. *IEEE Transactions on Neural Networks and Learning Systems*, 2022.

[5] Harold C Burger, Christian J Schuler, and Stefan Harmeling. Image denoising: Can plain neural networks compete with bm3d? In *2012 IEEE conference on computer vision and pattern recognition*, pages 2392–2399. IEEE, 2012.

[6] Zheng Chang, Xinfeng Zhang, Shanshe Wang, Siwei Ma, Yan Ye, Xiang Xinguang, and Wen Gao. Mau: A motion-aware unit for video prediction and beyond. In M. Ranzato, A. Beygelzimer, Y. Dauphin, P.S. Liang, and J. Wortman Vaughan, editors, *Advances in Neural Information Processing Systems*, volume 34, pages 26950–26962. Curran Associates, Inc., 2021.

[7] Tian Qi Chen, Yulia Rubanova, Jesse Bettencourt, and David K Duvenaud. Neural ordinary differential equations. In *Advances in Neural Information Processing Systems*, pages 6571–6583, 2018.

[8] Özgün Çiçek, Ahmed Abdulkadir, Soeren S. Lienkamp, Thomas Brox, and Olaf Ronneberger. 3d u-net: Learning dense volumetric segmentation from sparse annotation. In Sebastien Ourselin, Leo Joskowicz, Mert R. Sabuncu, Gozde Unal, and William Wells, editors, *Medical Image Computing and Computer-Assisted Intervention – MICCAI 2016*, pages 424–432, Cham, 2016. Springer International Publishing.

[9] Moshe Eliasof, Eldad Haber, and Eran Treister. Adr-gnn: Advection-diffusion-reaction graph neural networks. *arXiv preprint arXiv:2307.16092*, 2023.

[10] L. C. Evans. *Partial Differential Equations*. American Mathematical Society, San Francisco, 1998.

[11] Chelsea Finn, Ian Goodfellow, and Sergey Levine. Unsupervised learning for physical interaction through video prediction. *Advances in neural information processing systems*, 29, 2016.

[12] J. Fohring, E. Haber, and L. Ruthutto. Geophysical imaging of fluid flow in porous media. *SIAM J. on Sci. Comp*, to appar, 2014.

[13] Daniel Geng, Max Hamilton, and Andrew Owens. Comparing correspondences: Video prediction with correspondence-wise losses. In *Proceedings of the IEEE/CVF Conference on Computer Vision and Pattern Recognition*, pages 3365–3376, 2022.

[14] G.H. Golub and C.F. Van Loan. *Matrix Computations*. Johns Hopkins University Press, 1983.

[15] Ian Goodfellow, Jean Pouget-Abadie, Mehdi Mirza, Bing Xu, David Warde-Farley, Sherjil Ozair, Aaron Courville, and Yoshua Bengio. Generative adversarial nets. In *Advances in neural information processing systems*, pages 2672–2680, 2014.

[16] Jiuxiang Gu, Zhenhua Wang, Jason Kuen, Lianyang Ma, Amir Shahroudy, Bing Shuai, Ting Liu, Xingxing Wang, Gang Wang, Jianfei Cai, et al. Recent advances in convolutional neural networks. *Pattern recognition*, 77:354–377, 2018.

[17] Vincent Le Guen and Nicolas Thome. Disentangling physical dynamics from unknown factors for unsupervised video prediction. *2020 IEEE/CVF Conference on Computer Vision and Pattern Recognition (CVPR)*, pages 11471–11481, 2020.

[18] Eldad Haber, Keegan Lensink, Eran Treister, and Lars Ruthotto. Imexnet a forward stable deep neural network. In *International Conference on Machine Learning*, pages 2525–2534. PMLR, 2019.

[19] Kaiming He, Xiangyu Zhang, Shaoqing Ren, and Jian Sun. Deep residual learning for image recognition. In *Proceedings of the IEEE Conference on Computer Vision and Pattern Recognition*, pages 770–778, 2016.

[20] Jun-Ting Hsieh, Bingbin Liu, De-An Huang, Li F Fei-Fei, and Juan Carlos Niebles. Learning to decompose and disentangle representations for video prediction. *Advances in neural information processing systems*, 31, 2018.

[21] Xiaotao Hu, Zhewei Huang, Ailin Huang, Jun Xu, and Shuchang Zhou. A dynamic multi-scale voxel flow network for video prediction. In *Proceedings of the IEEE/CVF Conference on Computer Vision and Pattern Recognition*, pages 6121–6131, 2023.

[22] Nal Kalchbrenner, Aäron van den Oord, Karen Simonyan, Ivo Danihelka, Oriol Vinyals, Alex Graves, and Koray Kavukcuoglu. Video pixel networks. In *Proceedings of the 34th International Conference on Machine Learning*, volume 70 of *Proceedings of Machine Learning Research*, pages 1771–1779. PMLR, 2017.

[23] C.T. Kelley. *Iterative Methods for Linear and Nonlinear Equations*. SIAM, Philadelphia, 1995.

[24] Diederik P Kingma and Max Welling. Auto-encoding variational bayes. *arXiv preprint arXiv:1312.6114*, 2013.

[25] Alex Krizhevsky, Ilya Sutskever, and Geoffrey E Hinton. Imagenet classification with deep convolutional neural networks. In *Advances in neural information processing systems*, pages 1097–1105, 2012.

[26] Keegan Lensink, Bas Peters, and Eldad Haber. Fully hyperbolic convolutional neural networks. *Research in the Mathematical Sciences*, 9(4):60, 2022.

[27] M. Lentine, J. T. Gretarsson, and R. Fedkiw. An Unconditionally Stable Fully Conservative Semi-Lagrangian Method. *Journal of Computational Physics*, 230:2857–2879, 2011.

[28] R.J. LeVeque. *Numerical Methods for Conservation Laws*. Birkhauser, 1990.

[29] Siyuan Li, Zedong Wang, Zicheng Liu, Cheng Tan, Haitao Lin, Di Wu, Zhiyuan Chen, Jiangbin Zheng, and Stan Z Li. Moganet: Multi-order gated aggregation network. In *The Twelfth International Conference on Learning Representations*, 2023.

[30] Zewen Li, Fan Liu, Wenjie Yang, Shouheng Peng, and Jun Zhou. A survey of convolutional neural networks: analysis, applications, and prospects. *IEEE transactions on neural networks and learning systems*, 33(12):6999–7019, 2021.

[31] Zongyi Li, Nikola Kovachki, Kamyar Azizzadenesheli, Burigede Liu, Kaushik Bhattacharya, Andrew Stuart, and Anima Anandkumar. Fourier neural operator for parametric partial differential equations. *arXiv preprint arXiv:2010.08895*, 2020.

[32] Zongyi Li, Nikola Kovachki, Kamyar Azizzadenesheli, Burigede Liu, Andrew Stuart, Kaushik Bhattacharya, and Anima Anandkumar. Multipole graph neural operator for parametric partial differential equations. *Advances in Neural Information Processing Systems*, 33:6755–6766, 2020.

[33] Michael Mathieu, Camille Couprie, and Yann LeCun. Deep multi-scale video prediction beyond mean square error. *arXiv preprint arXiv:1511.05440*, 2015.

[34] Michael McCabe, Bruno Régaldo-Saint Blancard, Liam Holden Parker, Ruben Ohana, Miles Cranmer, Alberto Bietti, Michael Eickenberg, Siavash Golkar, Geraud Krawezik, Francois Lanusse, et al. Multiple physics pretraining for physical surrogate models. In *NeurIPS 2023 AI for Science Workshop*, 2023.

[35] J. Nagy and P.C. Hansen. *Deblurring Images*. SIAM, Philadelphia, 2006.

[36] Marc Oliu, Javier Selva, and Sergio Escalera. Folded recurrent neural networks for future video prediction. In *Proceedings of the European Conference on Computer Vision (ECCV)*, pages 716–731, 2018.

[37] Sergiu Oprea, Pablo Martinez-Gonzalez, Alberto Garcia-Garcia, John Alejandro Castro-Vargas, Sergio Orts-Escolano, Jose Garcia-Rodriguez, and Antonis Argyros. A review on deep learning techniques for video prediction. *IEEE Transactions on Pattern Analysis and Machine Intelligence*, 44(6):2806–2826, 2020.

[38] Keiron O'shea and Ryan Nash. An introduction to convolutional neural networks. *arXiv preprint arXiv:1511.08458*, 2015.

[39] Olaf Ronneberger, Philipp Fischer, and Thomas Brox. U-net: Convolutional networks for biomedical image segmentation. *CoRR*, abs/1505.04597, 2015.

[40] Lars Ruthotto and Eldad Haber. Deep neural networks motivated by partial differential equations. *arXiv preprint arXiv:1804.04272*, 2018.

[41] Lars Ruthotto and Eldad Haber. Deep neural networks motivated by partial differential equations. *Journal of Mathematical Imaging and Vision*, pages 1–13, 2019.

[42] Christian Schuldt, Ivan Laptev, and Barbara Caputo. Recognizing human actions: a local svm approach. In *Proceedings of the 17th International Conference on Pattern Recognition, 2004. ICPR 2004.*, volume 3, pages 32–36. IEEE, 2004.

[43] Minseok Seo, Hakjin Lee, Doyi Kim, and Junghoon Seo. Implicit stacked autoregressive model for video prediction. *arXiv preprint arXiv:2303.07849*, 2023.

[44] Junhong Shen, Liam Li, Lucio M. Dery, Corey Staten, Mikhail Khodak, Graham Neubig, and Ameet Talwalkar. Cross-modal fine-tuning: Align then refine. ICML, 2023.

[45] Xingjian Shi, Zhourong Chen, Hao Wang, Dit-Yan Yeung, Wai-kin Wong, and Wang-chun Woo. Convolutional lstm network: a machine learning approach for precipitation nowcasting. In *Proceedings of the 28th International Conference on Neural Information Processing Systems - Volume 1*, NIPS'15, page 802–810, Cambridge, MA, USA, 2015. MIT Press.

[46] Karen Simonyan and Andrew Zisserman. Very deep convolutional networks for large-scale image recognition. *arXiv preprint arXiv:1409.1556*, 2014.

[47] Makoto Takamoto, Timothy Praditia, Raphael Leiteritz, Dan MacKinlay, Francesco Alesiani, Dirk Pflüger, and Mathias Niepert. Pdebench: An extensive benchmark for scientific machine learning, 2023.

[48] Makoto Takamoto, Timothy Praditia, Raphael Leiteritz, Daniel MacKinlay, Francesco Alesiani, Dirk Pflüger, and Mathias Niepert. Pdebench: An extensive benchmark for scientific machine learning. *Advances in Neural Information Processing Systems*, 35:1596–1611, 2022.

[49] Cheng Tan, Zhangyang Gao, Siyuan Li, and Stan Z Li. Simvp: Towards simple yet powerful spatiotemporal predictive learning. *arXiv preprint arXiv:2211.12509*, 2022.

[50] Cheng Tan, Zhangyang Gao, Lirong Wu, Yongjie Xu, Jun Xia, Siyuan Li, and Stan Z Li. Temporal attention unit: Towards efficient spatiotemporal predictive learning. In *Proceedings of the IEEE/CVF Conference on Computer Vision and Pattern Recognition*, pages 18770–18782, 2023.

[51] Song Tang, Chuang Li, Pu Zhang, and RongNian Tang. Swinlstm: Improving spatiotemporal prediction accuracy using swin transformer and lstm. In *Proceedings of the IEEE/CVF International Conference on Computer Vision*, pages 13470–13479, 2023.

[52] Isabel Urbich, Jörg Bendix, and Richard Müller. A novel approach for the short-term forecast of the effective cloud albedo. *Remote Sensing*, 10(6):955, 2018.

[53] Ashish Vaswani, Noam Shazeer, Niki Parmar, Jakob Uszkoreit, Llion Jones, Aidan N Gomez, Łukasz Kaiser, and Illia Polosukhin. Attention is all you need. *Advances in neural information processing systems*, 30, 2017.

[54] Angel Villar-Corrales, Ani J. Karapetyan, Andreas Boltres, and Sven Behnke. Mspred: Video prediction at multiple spatio-temporal scales with hierarchical recurrent networks. In *British Machine Vision Conference*, 2022.

[55] Ruben Villegas, Jimei Yang, Seunghoon Hong, Xunyu Lin, and Honglak Lee. Decomposing motion and content for natural video sequence prediction. In *International Conference on Learning Representations*, 2017.

[56] Yunbo Wang, Zhifeng Gao, Mingsheng Long, Jianmin Wang, and Philip S Yu. PredRNN++: Towards a resolution of the deep-in-time dilemma in spatiotemporal predictive learning. In Jennifer Dy and Andreas Krause, editors, *Proceedings of the 35th International Conference on Machine Learning*, volume 80 of *Proceedings of Machine Learning Research*, pages 5123–5132. PMLR, 10–15 Jul 2018.

[57] Yunbo Wang, Lu Jiang, Ming-Hsuan Yang, Li-Jia Li, Mingsheng Long, and Li Fei-Fei. Eidetic 3d LSTM: A model for video prediction and beyond. In *International Conference on Learning Representations*, 2019.

[58] Yunbo Wang, Mingsheng Long, Jianmin Wang, Zhifeng Gao, and Philip S Yu. Predrnn: Recurrent neural networks for predictive learning using spatiotemporal lstms. In I. Guyon, U. Von Luxburg, S. Bengio, H. Wallach, R. Fergus, S. Vishwanathan, and R. Garnett, editors, *Advances in Neural Information Processing Systems*, volume 30. Curran Associates, Inc., 2017.

[59] Yunbo Wang, Jianjin Zhang, Hongyu Zhu, Mingsheng Long, Jianmin Wang, and Philip S Yu. Memory in memory: A predictive neural network for learning higher-order non-stationarity from spatiotemporal dynamics. In *Proceedings of the IEEE/CVF conference on computer vision and pattern recognition*, pages 9154–9162, 2019.

[60] Christopher K Wikle. Comparison of deep neural networks and deep hierarchical models for spatio-temporal data. *Journal of Agricultural, Biological and Environmental Statistics*, 24(2):175–203, 2019.

[61] Yue Wu, Qiang Wen, and Qifeng Chen. Optimizing video prediction via video frame interpolation. In *Proceedings of the IEEE/CVF Conference on Computer Vision and Pattern Recognition*, pages 17814–17823, 2022.

[62] Wei Xiong, Wenhan Luo, Lin Ma, Wei Liu, and Jiebo Luo. Learning to generate time-lapse videos using multi-stage dynamic generative adversarial networks. In *Proceedings of the IEEE Conference on Computer Vision and Pattern Recognition*, pages 2364–2373, 2018.

[63] Wei Yu, Yichao Lu, Steve Easterbrook, and Sanja Fidler. Efficient and information-preserving future frame prediction and beyond. In *International Conference on Learning Representations*, 2020.

[64] Junbo Zhang, Yu Zheng, and Dekang Qi. Deep spatio-temporal residual networks for citywide crowd flows prediction. In *Proceedings of the AAAI conference on artificial intelligence*, volume 31, 2017.

A Ablation Studies and Additional Experiments

A.1 Limited Generative Synthesis

Two real-life video datasets are taken to predict future time frames. Their statistics can be found in Table 7. The specific challenge posed by these datasets is due to the dissimilarity in the train and test sets. This is evident from the notable difference in the training and validation/test losses, which can be seen in Figure 6. The validation loss starts increasing with more epochs. For example, the KTH Action uses the movement behavior of 16 people for training while the models are tested on the movement behavior of 9 other people in a slightly altered scenario. So, we can say that the problem is to learn the general logic to predict unseen scenarios. Thus generative capability of a model could be crucial for better prediction.
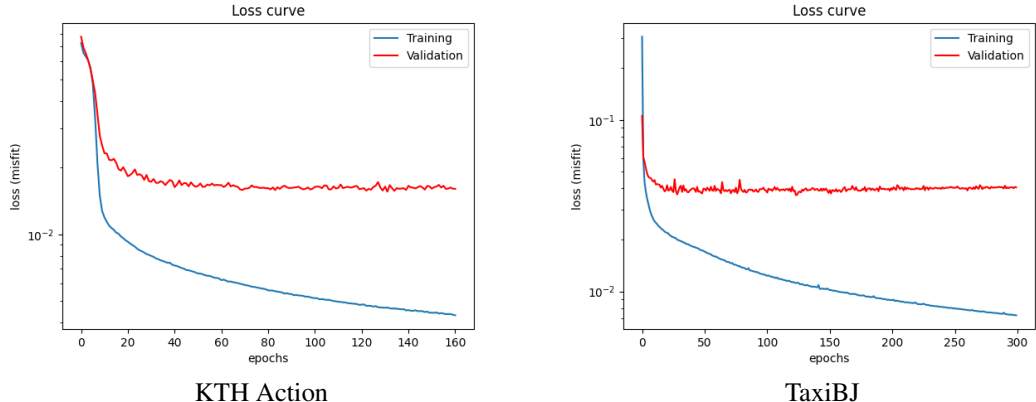

KTH Action	TaxiBJ

Figure 6: Bias in training and testing samples in KTH Action and TaxiBJ datasets

KTH Action   The KTH dataset features 25 individuals executing six types of actions: walking, jogging, running, boxing, hand waving, and hand clapping. Following methodologies established in references [55, 57], we utilize individuals 1-16 for training and individuals 17-25 for testing. The models are trained to predict the subsequent 20 frames based on the preceding 10 observations.

TaxiBJ   TaxiBJ is a collection of real-world GPS spatiotemporal data of taxis recorded as frames of 32x32x2 heat maps every half an hour, quantifying traffic flow in Beijing. We split the whole dataset into a training set and a test set as described in [64]. We train the networks to predict 4 future time frames from 4 observations.

Results   Our model is easily able to predict and outperform the state of art models in real-life video examples as well. The results for KTH Action and TaxiBJ can be seen in 8 and 9.

Table 7: Additional Dataset Statistics: Details on Training and Testing, Image Sequences, and Resolutions

Dataset	N_{train}	N_{test}	(C, H, W)	$History$	$Prediction$
KTH Action	5200	3167	(1, 128, 128)	10	20
TaxiBJ	19627	1334	(2, 32, 32)	4	4

A.2 CloudCast

The CloudCast dataset is used for multiple long-range predictions like 4, 8, 12, and 16 timesteps. It can be noticed that even if the MSE or the quality degrades, the degradation is noticeably minimal. It can be seen in Table 10, the figures for predicting 16 steps in future is still better than the state of art for 4 steps in future.

Table 8: Comparison of Our Method for KTH Action Dataset.

Method	SSIM ↑	PSNR (dB) ↑
ConvLSTM [45]	0.712	23.58
PredRNN [58]	0.839	27.55
CausalLSTM [56]	0.865	28.47
MSPred [54]	0.930	28.93
E3D-LSTM [57]	0.879	29.31
SimVP [49]	0.905	33.72
TAU [50]	0.911	34.13
SwinLSTM [51]	0.903	34.34
ADRNet	0.808	31.58

Table 9: Comparison of Our Method for TaxiBJ Dataset.

Method	MSE ↓	MAE ↓	SSIM ↑
ST-ResNet [64]	0.616	-	-
VPN [22]	0.585	-	-
ConvLSTM[45]	0.485	17.7	0.978
FRNN [36]	0.482	-	-
PredRNN [58]	0.464	17.1	0.971
CausalLSTM [56]	0.448	16.9	0.977
MIM [59]	0.429	16.6	0.971
E3D-LSTM [57]	0.432	16.9	0.979
PhyDNet [17]	0.419	16.2	0.982
SimVP [49]	0.414	16.2	0.982
SwinLSTM [51]	0.390	-	0.980
IAM4VP [43]	0.372	16.4	0.983
TAU [50]	0.344	15.6	0.983
ADRNet	0.445	16.6	0.975

Table 10: Results for CloudCast dataset. Comparison of our model (ADRNet) with state of art models

ADRNet Predictive performance				
Metric	t + 4	t + 8	t + 12	t + 16
MSE (↓)	0.015	0.016	0.018	0.019
SSIM (↑)	0.83	0.79	0.76	0.74
PSNR (↑)	38.17	37.89	37.35	37.23

B Evaluation Metrics

Moving MNIST, KTH Action, TaxiBJ, CloudCast These specific video prediction datasets have been using MAE (Mean Absolute Error), MSE (Mean Squared Error), SSIM (Structural Similarity) and PSNR (Peak Signal-to-Noise Ratio). The evaluated SSIM and PSNR are averaged over each image. The MSE and MAE have a specific way to calculate, where the pixel-wise evaluation values are summed up for all the pixels in the image.

$$\text{MSE} = \frac{1}{N} \sum_{i=1}^{N} \sum_{h=1}^{H} \sum_{w=1}^{W} \sum_{c=1}^{C} (y - \hat{y})^2 \tag{16}$$

$$\text{MAE} = \frac{1}{N} \sum_{i=1}^{N} \sum_{h=1}^{H} \sum_{w=1}^{W} \sum_{c=1}^{C} |y - \hat{y}| \tag{17}$$

$$\text{PSNR} = \frac{1}{N}\sum_{i=1}^{N} 10 \cdot \log_{10}\left(\frac{\text{MAX}^2}{\text{MSE}}\right) \tag{18}$$

$$\text{SSIM(x,y)} = \frac{(2\mu_x\mu_y + C_1)(2\sigma_{xy} + C_2)}{(\mu_x^2 + \mu_y^2 + C_1)(\sigma_x^2 + \sigma_y^2 + C_2)} \tag{19}$$

$$\overline{\text{SSIM}} = \frac{1}{N}\sum_{i=1}^{N} \text{SSIM}(x, y) \tag{20}$$

where:

N is the number of images in the dataset,

H is the height of the images,

W is the width of the images,

C is the number of channels (e.g., 3 for RGB images),

y is the true pixel value at position (i, h, w, c), and

$\hat{y}$ is the predicted pixel value at position (i, h, w, c).

MAX is the maximum possible pixel value of the image (e.g., 255 for an 8-bit image),

MSE is the Mean Squared Error between the original and compressed image.

μ_x is the average of x,

μ_y is the average of y,

σ_x^2 is the variance of x,

σ_y^2 is the variance of y,

σ_{xy} is the covariance of x and y,

$C_1 = (K_1 L)^2$ and $C_2 = (K_2 L)^2$ are two variables to stabilize the division with weak denominator,

L is the dynamic range of the pixel values (typically, this is 255 for 8-bit images),

K_1 and K_2 are small constants (typically, $K_1 = 0.01$ and $K_2 = 0.03$).

PDEBench-SWE PDEBench uses the concept of pixel-wise mean squared error (MSE) and normalized mean squared error (nMSE) to validate scaled variables in simulated PDEs. Along with these, we also use root mean squared error (RMSE) and normalized root mean squared error (nRMSE).

$$\text{MSE} = \frac{1}{N \cdot H \cdot W \cdot C}\sum_{n=1}^{N}\sum_{h=1}^{H}\sum_{w=1}^{W}\sum_{c=1}^{C}(x - \hat{x})^2 \tag{21}$$

$$\text{nMSE} = \frac{1}{N \cdot H \cdot W \cdot C}\sum_{n=1}^{N}\sum_{h=1}^{H}\sum_{w=1}^{W}\sum_{c=1}^{C}\frac{(x - \hat{x})^2}{x^2} \tag{22}$$

$$\text{RMSE} = \frac{1}{N}\sqrt{\frac{1}{H \cdot W \cdot C}\sum_{n=1}^{N}\sum_{h=1}^{H}\sum_{w=1}^{W}\sum_{c=1}^{C}(x - \hat{x})^2} \tag{23}$$

$$\text{nRMSE} = \frac{1}{N}\sqrt{\frac{1}{H \cdot W \cdot C}\sum_{n=1}^{N}\sum_{h=1}^{H}\sum_{w=1}^{W}\sum_{c=1}^{C}\frac{(x - \hat{x})^2}{x^2}} \tag{24}$$

where:

N is the number of images in the dataset,

H is the height of the images,

W is the width of the images,

C is the number of channels (e.g., 3 for RGB images),

x is the true pixel value at position (n, h, w, c), and

$\hat{x}$ is the predicted pixel value at position (n, h, w, c).

KITTI

$$\text{MS-SSIM}(x, y) = [l_M(x, y)]^{\alpha_M} \prod_{j=1}^{M} [c_j(x, y)]^{\beta_j} [s_j(x, y)]^{\gamma_j} \tag{25}$$

$$\overline{\text{MS-SSIM}} = \frac{1}{N} \sum_{i=1}^{N} \text{MS-SSIM}(x, y) \tag{26}$$

where:

N is the number of images in the dataset,

$l_M(x, y)$ is the luminance comparison at the coarsest scale M,

$c_j(x, y)$ is the contrast comparison at scale j,

$s_j(x, y)$ is the structure comparison at scale j,

$\alpha_M, \beta_j, \gamma_j$ are the weights applied to the luminance, contrast, and structure terms at each scale respectively,

M is the number of scales used in the comparison.

The luminance, contrast, and structure comparisons are given by:

$$l(x, y) = \frac{2\mu_x \mu_y + C_1}{\mu_x^2 + \mu_y^2 + C_1}$$

$$c(x, y) = \frac{2\sigma_x \sigma_y + C_2}{\sigma_x^2 + \sigma_y^2 + C_2}$$

$$s(x, y) = \frac{\sigma_{xy} + C_3}{\sigma_x \sigma_y + C_3}$$

where:

μ_x, μ_y are the local means of x and y,

σ_x, σ_y are the local standard deviations of x and y,

σ_{xy} is the local covariance of x and y,

C_1, C_2, C_3 are constants to stabilize the division.

$$\text{LPIPS}(x, \hat{x}) = \sum_l \frac{1}{H_l W_l} \sum_{h=1}^{H_l} \sum_{w=1}^{W_l} \|w_l \odot (\phi_l(x)_{hw} - \phi_l(\hat{x})_{hw})\|_2^2 \tag{27}$$

$$\overline{\text{LPIPS}} = \frac{1}{N} \sum_{i=1}^{N} \text{LPIPS}(x, \hat{x}) \tag{28}$$

where:

N is the number of images in the dataset,

$\phi_l(x)$ is the activation of the l-th layer of a deep network for the image x,

$\phi_l(\hat{x})$ is the activation of the l-th layer of a deep network for the image $\hat{x}$,

w_l is a learned weight vector for the l-th layer,

H_l and W_l are the height and width of the l-th layer activations,

$\odot$ denotes element-wise multiplication.

C   Hyperparameter Settings and Computational Resources

C.1   ADRNet Training on PDEBench-SWE

Hyperparameter	Symbol	Value
Learning Rate	η	$1e-04$
Batch Size	B	64
Number of Epochs	N	200
Optimizer	-	Adam
Number of Layers	-	1
Hidden Channels	-	128
Activation Function	-	SiLU

Table 11: Neural Network Hyperparameters

C.2   ADRNet Training on Other Datasets

Hyperparameter	Symbol	Value
Learning Rate	η	$2e-06$
Batch Size	B	16
Number of Epochs	N	1000
Optimizer	-	Adam
Number of Layers	-	8
Hidden Channels	-	192
Activation Function	-	SiLU
Learning Rate Scheduler	-	ExponentialLR

Table 12: Neural Network Hyperparameters

C.3   Computational Resources

All our experiments are conducted using an NVIDIA RTX-A6000 GPU with 48GB of memory.